



Supplementary Materials for

Ultrafast disordering of vanadium dimers in photoexcited VO₂

Simon Wall, Shan Yang, Luciana Vidas, Matthieu Chollet, Michael Glowonia, Michael Kozina, Tetsuo Katayama, Thomas Henighan, Mason Jiang, Timothy A. Miller, David A. Reis, Lynn A. Boatner, Olivier Delaire, Mariano Trigo

Correspondence to: simon.wall@icfo.eu olivier.delaire@duke.edu mtrigo@slac.stanford.edu

This PDF file includes:

Materials and Methods
Supplementary Text
Figs. S1 to S12
Captions for Movies S1 to S2
Supplementary references 31-48

Other Supplementary Materials for this manuscript include the following:

Movies S1 to S2

Materials and Methods

Experimental setup

Measurements were performed at the XPP endstation (31) of the Linac Coherent Light Source (LCLS). A single crystal of VO₂ was mounted on a copper block attached to a heating stage and enclosed in a helium purge box to reduce air scattering. The sample normal is along the [110] rutile direction and we define the azimuth $\phi = 0$ corresponding to the beam incident along the rutile *c*-axis. The X-rays were monochromatized to ~ 1 eV bandwidth using a diamond 111 double crystal tuned to 9.5 keV. A sketch of the experimental geometry is shown in Fig S1. The pump laser pulses from a regenerative Ti:Sapphire amplifier had a central wavelength of 800 nm and a pulse duration of 45 fs at the sample position. Time resolved measurements were performed for two sample orientations, $\phi = 7$ deg shown in Figure 2 and $\phi = 22$ deg. In order to match the penetration depths of the pump and probe beams, a grazing incidence geometry was adopted. The X-rays were incident at 0.5 degrees and the pump beam impinged on the sample at an angle of 2.3 degrees and was focused to a transverse spot size of 0.13 mm x 0.5 mm. The scattered X-rays were detected with the large area Cornell-SLAC Pixel Array Detector (CSPAD). A ~ 3 mm thick plexiglass sheet was placed in front of the detector to suppress the vanadium fluorescence near 5 keV. The detector distance, ~ 120 mm, was calibrated using the powder diffraction rings from a LaB₆ polycrystalline sample. In the pump probe measurements, the laser was electronically delayed to -11 nanoseconds every 3rd pulse to track drifts in the pre-time zero signal.

As indicated in Fig S1, the pump beam slightly overfilled the sample surface due to the grazing incidence geometry employed. This resulted in some intensity falling on the surface normal to the propagation direction. Due to the high pump fluences required to drive the phase transition with a grazing geometry, the fluence on this surface is high, and resulted in some sample damage. This damaged region resulted was also probed by the tail of the X-ray beam and is responsible for the diffraction rings observed in Fig 2.

In order to avoid damaging the CSPAD with strong diffracted beams, the measurements were performed with the sample rotated slightly off from the ideal Bragg conditions. Even though the geometry is such that the Bragg condition is not strictly satisfied, the structure factor is a slow function of \mathbf{Q} , and the dynamics of these pixels is representative of the respective structure factors at the Bragg condition. To verify this, we also performed a rocking curve measurement at the SACLA FEL (Fig. S7) showing that there is no shifts associated with strain on the timescales considered in this paper.

Fluence calculation

The laser pulse energy (E_p) was controlled by a combination of waveplate and polarizer and measured with a power meter. As measurements were performed in a grazing geometry, the laser was focused by two cylindrical lenses of different focal lengths in order to produce an elliptical projection of the beam on the sample surface. The spot size, measured in the focus but normal to the beam propagation direction, was 0.13 mm x 0.5 mm, the values correspond to the FWHM of the beam intensity. The laser impinged on the sample with an angle of 2.3 degrees relative to the sample surface. This results in a projected area $A = \pi * 0.013 * 0.05 / (4 * \sin(2.3^\circ)) \text{cm}^2$. The reflectivity of the sample was also accounted for in order to obtain the absorbed fluence. The

samples were measured with ellipsometry to obtain the complex refractive index $n(800\text{ nm}) = 2.45 + 1.06i$. The value is in good agreement with the literature (32). This results in a reflectivity of $R_p = 0.665$ for p-polarized light at 2.3° to the sample surface. The reported fluence is then $F = (1 - R_p)E_p/A$. The threshold of 4 mJ/cm^2 obtained is within the range of values reported in the literature.

Sample Synthesis

Single crystals of vanadium dioxide (VO_2) were grown by means a crystallization technique incorporating some aspects of “self-fluxing”. The VO_2 growth was carried out by first placing high-purity V_2O_5 in a rectangular quartz boat. The quartz boat containing the V_2O_5 charge was placed inside a larger quartz tube with one end of the tube closed. The boat and single-closed-end tube were then placed in a horizontal tube furnace that incorporated a quartz tube-furnace liner. The sealed end of the larger diameter tube containing the quartz boat and growth charge was oriented toward the direction of an Argon gas flow. To initiate the growth process, the quartz furnace-liner tube was evacuated and purged with Ar several times, and a continuous flow of Ar was then established. At this point, the temperature in the horizontal tube furnace was set at 1000 C and maintained at this temperature for approximately 120 h . After 120 h , the furnace was turned off, the system was allowed to cool to room temperature while maintaining an Ar gas flow, the quartz boat was removed from the furnace, and the resulting VO_2 crystals were harvested. The resulting VO_2 samples are highly aligned single-domain crystals in the rutile phase and exhibit twin domains in the monoclinic M1 phase.

AIMD Simulations

Ab-initio molecular dynamics simulations were performed within the framework of the Vienna Ab initio Simulation Package (VASP) (33,34). The calculations used projector augmented-wave potentials (35,36), with a cutoff energy of 500 eV . Most calculations used a $2\times 2\times 2$ supercell of the M1 conventional unit cell, although additional calculations were performed on a $2\times 2\times 5$ supercell of the rutile phase. Most of the AIMD calculations were performed with the PBE exchange-correlation function with a Hubbard U correction on d-electrons of V atoms, with $U=4.2\text{eV}$ and $J=0.8\text{eV}$ (21,37,38). The occupancy of electronic states was set using Fermi-Dirac statistics at chosen electronic temperatures. The AIMD simulations of the photoexcitation were conducted by first running the system at constant temperature ($T=300\text{K}$) and constant volume equilibrium ensemble (NVT), starting with the M1 crystal structure obtained from a structural relaxation. The AIMD simulation time step was 1fs . After equilibration for several picoseconds, the effect of laser photoexcitation was simulated by suddenly increasing the electronic temperature in the Fermi-Dirac distribution. The volume of the system was kept constant, since experimentally the volume cannot respond on ultrafast time scales. After the photoexcitation, the ensemble was switched from (NVT) to (NVE), with an increased electronic temperature, corresponding to increasing the electronic distribution width $\sigma = k_B T_{el}$ from 0.025eV ($T_{el} \sim 290\text{K}$) to 0.19 eV ($T_{el} \sim 2204\text{K}$). After photoexcitation, the structure is observed to change to a rutile-like structure, through the disappearance of the dimerization, while the initial monoclinic lattice parameters are kept fixed. The electronic temperature was chosen based on our study of the evolution of the static ground state structure upon varying the electronic occupations (Fig. S4). The calculated quantities were averaged for 10 different initial thermal states in order to achieve good sampling of the dynamics.

Separate AIMD simulations of the equilibrium rutile structure were performed with a 2x2x5 tetragonal supercell at constant temperature ($T=380\text{K}$), under constant volume equilibrium ensemble (NVT). The phonon DOS for different simulated conditions were obtained by taking the FFT of the velocity correlation function from AIMD trajectories. See supplementary material for additional details.

Bragg peak intensity simulations

In the monoclinic M1 phase, four possible twins can occur (illustrated in Fig. S8), Our experiments were performed on a region of the sample containing only one pair of twins, corresponding to 180° rotation about the rutile c axis. Consequently, the calculation of Bragg peak intensities were obtained by averaging the corresponding Bragg reflections of the two twins. Also 10 random trajectories were added together to increase the statistics. The simulations were also convolved with the experimental resolution of 50 fs (Fig. S9)

Photoexcited potential

In Fig 4c, the distortions at which the potential energy was evaluated were obtained from a linear combination of the eigenvectors belonging to the lowest two degenerate modes at the R point of the rutile phase (Fig. S6(d)). The distortions were imposed to the rutile supercell to obtain the distorted structures, and the energy was evaluated for each distortion amplitude. The calculation was repeated for two different electronic temperatures.

Supplementary Text

General parameters and convergence

All the density functional simulations were performed with the Vienna Ab initio Simulation Package (VASP) (33,34), using projector augmented-wave potentials (35,36), and the PBE (37) exchange-correlation functional, with Hubbard correction in the case of the M1 phase. $V(3s^23p^64s^23d^3)$ and $O(2s^22p^4)$ were treated as valence electrons in the PAW potential, with an energy cut-off of 500eV in all the calculations.

Structure relaxation and static photo-excitation

The structure of the M1 phase was fully relaxed by using a conventional unit cell and PBE+U, with $U=4.2$ eV and $J=0.8$ eV used to describe electronic correlations of the V 3d electrons (21,38). The K-point mesh used was a Γ -centered $8\times 8\times 8$ mesh. The electronic partial occupancy was controlled by the Fermi-Dirac statistics, $\sigma = k_B T_{el} = 0.025eV$ ($T_{el} \sim 290K$). The residual forces on atoms were converged to less than $1\text{meV}/\text{\AA}$. The resulting lattice constants are $a=5.62$ \AA, $b=4.61$ \AA and $c=5.43$ \AA, and $\beta=121.81^\circ$, in good agreement with experimentally reported lattice constants in the M1 phase at $T=298\text{K}$ $a=5.75$ \AA, $b=4.54$ \AA, $c=5.38$ \AA and $\beta=122.65^\circ$ (39).

The rutile phase was fully relaxed by using conventional unit cell within PBE (37) (no Hubbard correction). The electron partial occupancy was controlled by Fermi-smearing $\sigma = 0.033\text{eV}$ ($T_{el} \sim 380\text{K}$). The forces were converging to $0.1\text{meV}/\text{\AA}$, with $4\times 4\times 8$ Γ -centered K-points. The resulting lattice constants are $a=4.60\text{\AA}$, and $c=2.80\text{\AA}$ in good agreement with experimentally reported lattice constants in the rutile phase at $T=360\text{K}$ with $a=4.55\text{\AA}$, $c=2.85\text{\AA}$ (40).

The effect of photo-excitation on the structure of the M1 phase was studied by varying the electronic occupation smearing parameter σ and relaxing the atomic positions, while keeping the lattice parameters fixed to the relaxed values of the M1 phase, as determined above. The effect of the electronic occupation smearing parameter (Fermi-Dirac partial occupations) on the structure of the M1 phase was investigated by varying the width of Fermi-smearing function, with a series of increasing values of $\sigma = kT$. The energy was converging to 10^{-6}eV , using an $8\times 8\times 8$ Γ -centered k -point mesh. The evolution of the bond lengths and twisting angles as function of increasing σ are shown in Fig. S4(a,b).

In Fig. S4(a) the short and long V-V bonds suddenly collapse to an identical value for $\sigma \geq 0.25\text{eV}$, ($T_{el} \sim 2900\text{K}$) which is consistent with the first-order nature of the phase transition. At the same $\sigma = 0.25\text{eV}$ ($T_{el} \sim 2900\text{K}$), the twisting angles become 180° Fig. S4(b). All these illustrate that the M1 structure abruptly becomes rutile-like above a critical smearing of electronic occupations, $\sigma_c = 0.25\text{eV}$, $T_{el} \sim 2900\text{K}$).

Lattice dynamics:

The phonon density of states (PDOS) and dispersions for the M1 phase were calculated from first-principles, using the atomic forces from VASP calculations, and the small displacement method as implemented in Phonopy (41), under the harmonic approximation. A $2\times 2\times 2$ supercell (96 atoms), based on the M1 fully relaxed unit cell, was used for phonon dispersion calculation. The energy was converging to 10^{-6}eV for each distorted supercell structure, with Γ centered $4\times 4\times 4$ K-points. The phonon calculations for the M1 phase used the PBE+U scheme with $U=4.2\text{eV}$ and $J=0.8\text{eV}$. Results are shown in Fig. S6(a)(c).

The phonon DOS and dispersions for the rutile phase were calculated with the TDEP method, with anharmonic effects included in renormalized harmonic force constants (42). The renormalized harmonic force constants were extracted from the ab initio molecular dynamics (AIMD) performed at $T = 380\text{K}$ with PBE and the recommended smearing method for metallic phase (Methfessel-Paxton order 1). The results, shown in Fig. S6(b)(d), are in good agreement with prior reports (21, 43). Comparing Fig. S6(a) and S6(b), a clear peak is seen at 3 THz in the V-projected phonon DOS for the rutile phase, but absent in the M1 phase, corresponding to flat transverse acoustic and optic dispersion branches around 3 THz across extended portions of the Brillouin zone, as seen in Fig. S6(d). The M1 phase is characterized by overall stiffer bonding, reflected in larger phonon frequencies.

Distortion potential:

The total energies of a series of displacements were calculated with electronic occupation smearing parameter $\sigma = 0.025\text{eV}$ ($T_{el} \sim 290\text{K}$) and $\sigma = 0.19\text{eV}$ ($T_{el} \sim 2204\text{K}$) with the PBE+U scheme ($U=4.2\text{eV}$ and $J=0.8\text{eV}$) and $8 \times 4 \times 8$ Γ centered K-points (21,38). The distortion potential was calculated based on the $1 \times 2 \times 2$ supercell (24 atoms) of the relaxed rutile phase, and incorporated the modulation at the R point shown in Fig. S6(d). This distortion results from the linear combination of the eigenvectors belonging to the lowest two degenerate (transverse acoustic) modes at the R point of the rutile Brillouin zone. The calculation results are shown in Figure. 4(b) of the main text. In this figure, the potential changes from a double-well to a single flat well (at zero distortion) when $\sigma = 0.19\text{eV}$ ($T_{el} \sim 2204\text{K}$), which explains the occurrence of the structural phase transition upon photo-excitation. The appearance of the 3THz peak of the V PDOS in the rutile phase is also due to the flatness of the potential, comparing with the M1 phase equilibrium potential.

Ab initio molecular dynamics

Ab initio molecular dynamics (AIMD) calculations for M1 used a $2 \times 2 \times 2$ supercell (96 atoms) constructed from the fully relaxed conventional unit cell. The Γ only K-points and plane wave cut-off energy 500 eV were still used throughout the AIMD calculations for M1. The PBE+U exchange correlation was used before and after photo-excitation, with $U = 4.2$ eV and $J = 0.8$ eV (21, 38). The time step was 1 fs. The electron partial occupancy was controlled by the Fermi smearing method, as above. Ten parallel random trajectories were used in the simulation to increase the statistics.

Before photo-excitation, the calculations were performed under a canonical ensemble (NVT) with Nose-Hoover thermostat. The system was thermalized for 4 ps to 5 ps at $T_{ion} = 300\text{K}$, under canonical ensemble (NVT) with the electronic occupation smearing parameter at $\sigma = 0.025$ ($T_{el} \sim 290\text{K}$). The volume of the system was kept constant before and after photoexcitation, as thermal expansion occurs in a time-scale of many picoseconds, and is not considered here. In the experiment, the energy was injected to the system by a femtosecond pump laser, and no energy exchange between the sample and the environment occurs within the first picoseconds. Thus, the ensemble after photo-excitation was switched to a microcanonical ensemble (NVE), with the structural configuration from the last step of the NVT AIMD calculation. At the same time, to simulate the laser pump, σ was set to 0.19 eV ($T_{el} \sim 2204\text{K}$).

AIMD for the rutile phase was based on a $2 \times 2 \times 5$ supercell (120 atoms) of the conventional unit cell. The exchange correlation functional used was PBE, with a 500 eV energy cut-off. The time step was 1fs, and the system was equilibrated for 4 ps to 5 ps. The AIMD calculations for the equilibrium rutile phase were performed under a canonical ensemble (NVT) with Nose-Hoover thermostat at 380K. The electronic occupation smearing parameter σ was set to 0.033 eV, to match the lattice temperature ($T_{el} = T_{ion} = 380\text{K}$). Ten parallel random trajectories were used in the simulation.

Diffraction structure factor and intensity:

The structure factors were calculated as $F(h, k, l) = f_v \sum_v e^{iq(h,k,l) \cdot r_v(t)} + f_o \sum_o e^{iq(h,k,l) \cdot r_o(t)}$ with atomic form factors $f_v = 23$ and $f_o = 8$. In the structure factor, $q(h,k,l)$ denotes the wave-vector, and $r(t)$ is the atomic position of either V or O atoms at time t (44). Structure factors were calculated for each time step with the atomic positions taken from independent AIMD trajectories. The diffraction intensity was obtained as $I(h, k, l) = |F(h, k, l)|^2$ at each time step. Subsequently, the computed intensity from ten independent trajectories were added together. In order to improve the signal-to-noise ratio, the intensity in Fig. 3(b) and Fig.S10 shows the average of the corresponding Bragg peaks from the two accessible twins in the experimental geometry (twin1 and twin2) (related by a 180° rotation about the rutile c -axis, as shown in Fig. S8(a)).

Atomic displacements:

The displacements are the amplitude of the displacements of (N=32) V atoms in the supercell.

$$\text{Displacement} = \sum_i^N |x_i - x_0|$$

The reference configuration was chosen as the fully relaxed M1 atomic positions of V atoms. The V displacements of 10 parallel trajectories were taken together. The mean displacement was calculated by taking the statistical mean value of all the displacements. The standard deviation was the standard deviation of all the displacements obtained by statistical model, shown in Fig. 3(b) (main text).

Bond length and twisting angle:

The length of five short V-V bonds and five long V-V bonds were extracted from the supercell in each time step of each AIMD trajectory. All the short and long bond lengths for the ten trajectories are plotted together in Fig. 4(a) (main text), with light red lines representing all the short bonds and light blue lines are for all the long bonds. The thick red line stands for the average of the short bonds in the supercell in all the trajectories. The thick blue line is for the corresponding long bonds. The twisting angles were calculated from the angles between adjacent V-V short bonds and V-V long bonds. Ten twisting angles were calculated from each supercell, and all the corresponding angles from the ten trajectories were presented in Fig. S5(a) with black lines. The red line in Fig. S5(a) is the average of all the twisting angles. The bond lengths Figure. 4(a) (main text) and twisting angles from AIMD behave consistent with static bond length and bond angle calculations, shown in Fig. S4(a,b).

Phonon density of states:

The PDOS in Fig. 4(d)(main text) was obtained from the fast Fourier transform (FFT) of the velocity autocorrelation function, as implemented in nMOLDYN (45). The velocities were obtained from finite differences of the atomic positions in AIMD trajectories. In Figure. 4(d), the PDOS for the equilibrium M1 phase at 300 K was obtained over the time window, $-1000 < t < 0$ fs before the photo-excitation (photoexcitation occurs at $t=0$ fs). For the PDOS of the photoexcited phase, a time window of $0 < t < 1000$ fs was used. Both for the equilibrium M1 phase and the photoexcited phase, ten separate AIMD trajectories were added together to improve the statistics of the phonon DOS. In addition, the PDOS for the equilibrium rutile phase was obtained using the

same method, with ten independent AIMD trajectories, each 1000 fs long, performed at $T_{ion} = 380$ K, ($T_{el} \sim 380K$).

The PDOS Figure. 4(d) (main text) shows PDOS before photo-excitation in M1 phase, which is similar to the PDOS with harmonic approximation in Fig. S6(a). The PDOS of M1 at $0 < t < 1000$ fs in Figure. 4(d), shows a peak at 3THz. This peak position is similar with the 3THz phonon peak in equilibrium rutile phase in Figure. 4(d) (main text) and in Fig. S6(b). The similarities in the PDOS indicate that the atomic dynamics become similar to those in the equilibrium rutile phase within 1ps.

Fig. S1.

Experimental schematic. In order to match pump and probe penetration depths, a grazing incidence geometry was adopted. This results in an overfilling of the sample surface with the pump laser beam. This results in front surface experiencing a high fluence and laser induced damage, which generated the ring structure in Fig 2. Rotations around ϕ , enable us to measure different regions of the total scattering. Upper left insert shows a polarized light microscopy image of the VO₂ single-crystal used. Light/dark patches correspond to different M1 twin domains.

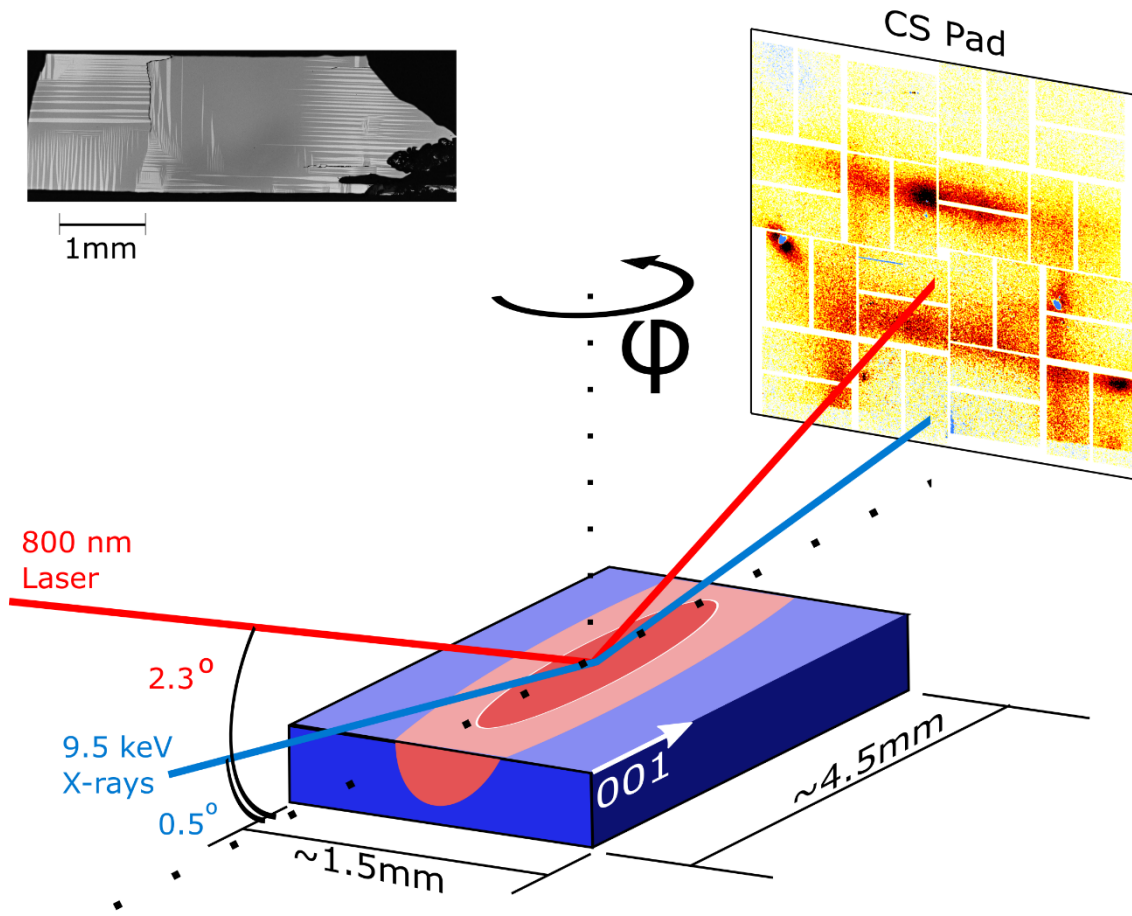


Fig. S2.

Comparison of the equilibrium diffuse scattering. Measured M1 phase ($\phi = 7^\circ$ and $T = 295$ K) (a) and R phase ($\phi = 7^\circ$ and $T = 353$ K) (c), together with the simulated scattering patterns for the M1 (b) and R phase (d). Solid lines in the simulation represent the Brillouin zone boundaries of the rutile phase.

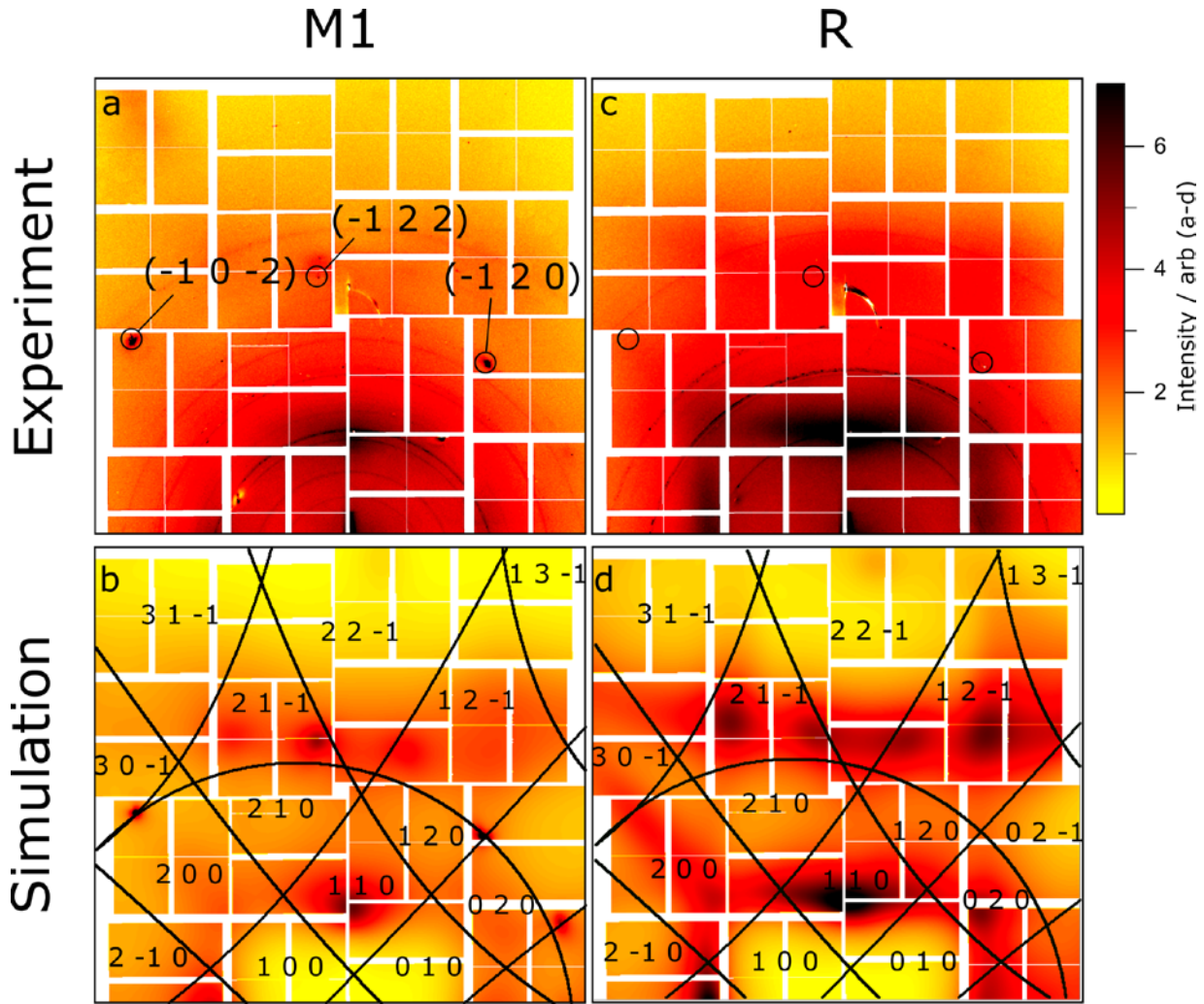


Fig. S3.

Diffuse scattering of the M1 phase for $\phi = 22^\circ$. This orientation was used to obtain the dynamics of the other diffraction peaks plotted in Fig 3.

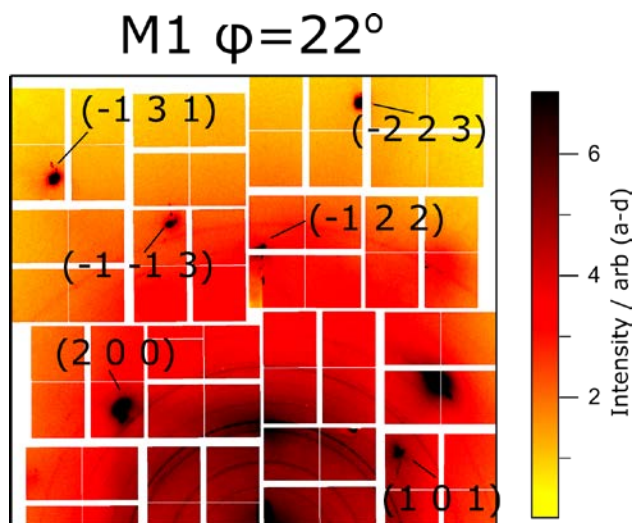


Fig. S4.

Evolution of V-V bond lengths and twisting angle in M1 VO₂ as a function of the electronic occupation smearing parameter, $\sigma = k_B T_{el}$. a. Bond lengths of long and short V pairs as a function of σ . b. Twisting angles between V short and long bonds as a function of σ . For $\sigma \geq 0.25 eV$ ($T_{el} \sim 2900 K$), the short and long V bonds collapse to the same bond length, and the twisting angle becomes 180°.

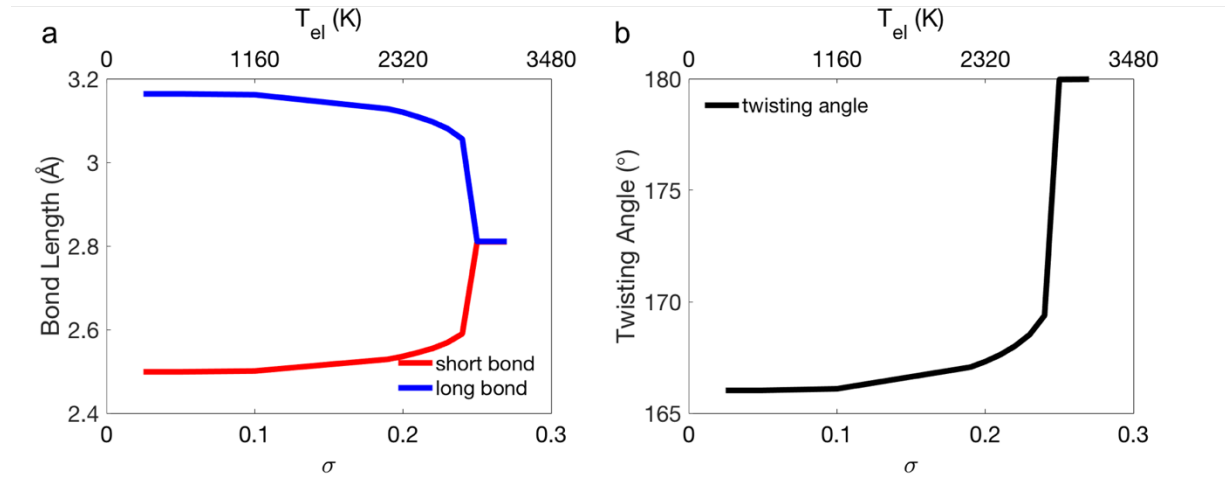


Fig. S5.

Statistical Analysis of bond angles and bond lengths. (a) Twisting angles in the AIMD before and after photo-excitation. (b) FFT of long and short bond lengths from Figure. 4(a) after 0 fs.

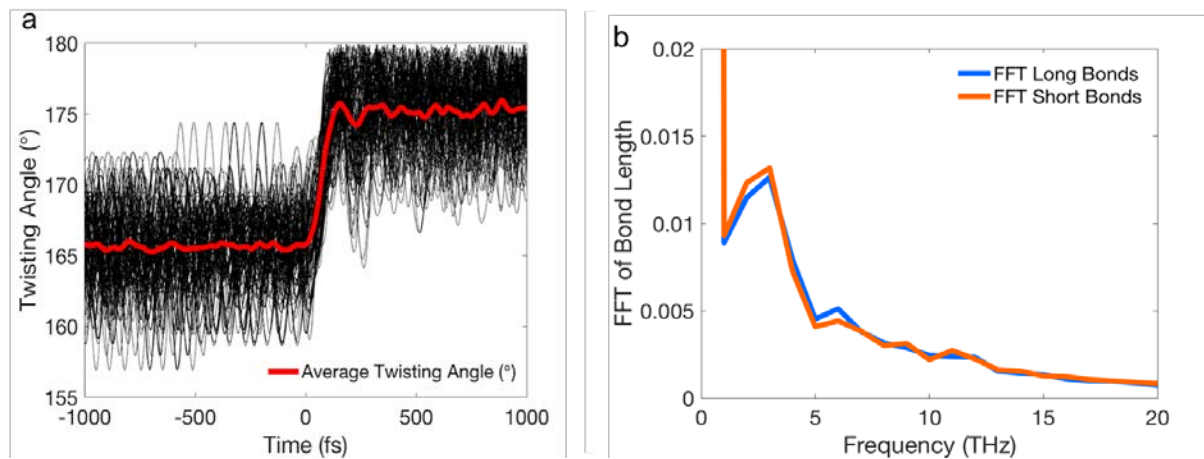


Fig. S6.

Phonon density of states and Phonon dispersions of VO₂ for M1 and R phases. (a,c) Phonon DOS and phonon dispersions of M1 phase, from first-principles lattice dynamics within the harmonic approximation. Labels of high-symmetry points for the wave-vector are given for both M1 setting and the equivalent rutile coordinate in parentheses. (b,d) Phonon DOS and phonon dispersions for rutile VO₂, computed using renormalized effective harmonic force constants from AIMD at T=380K, derived with the TDEP method.

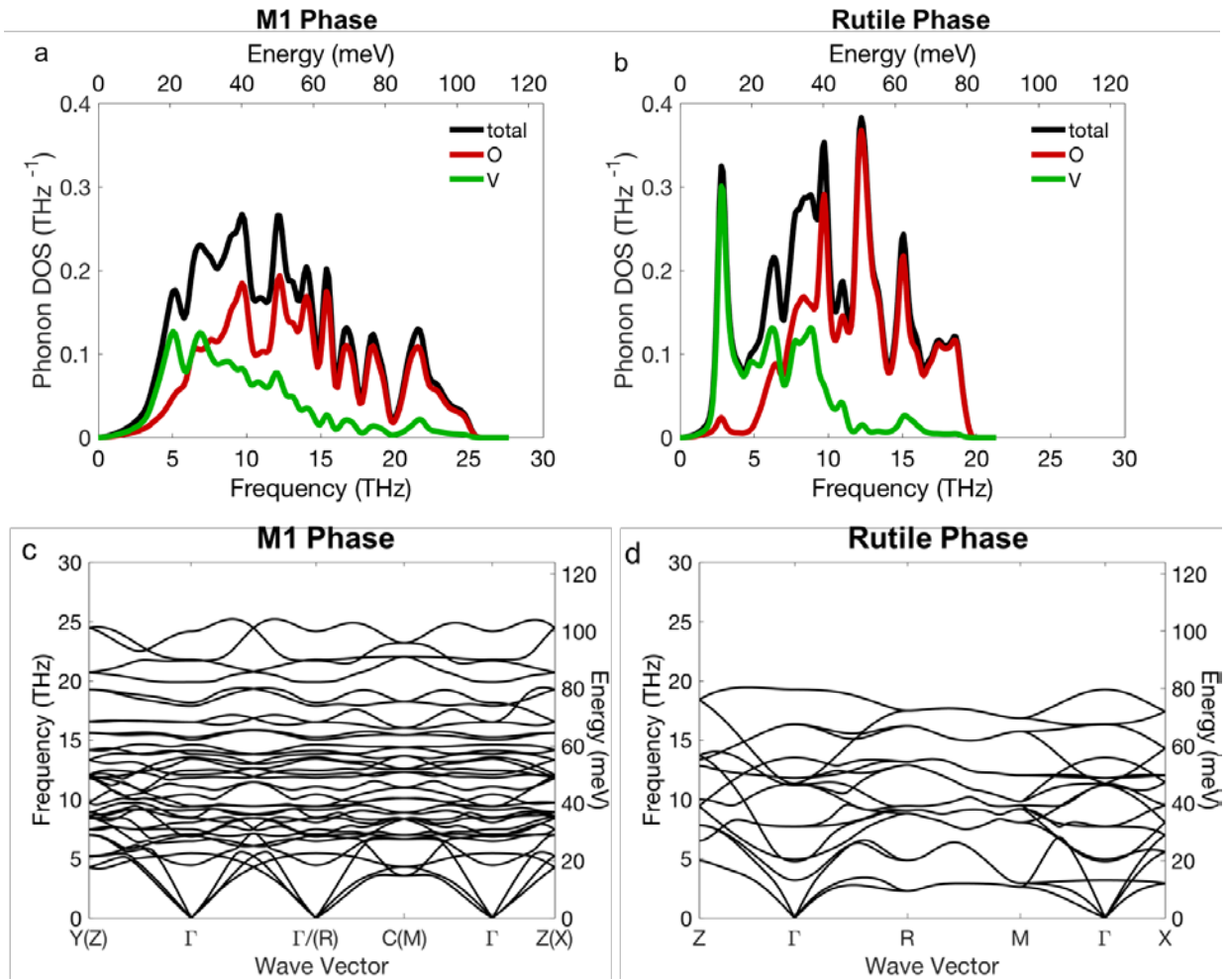


Fig. S7.

Transient rocking curve measured at the SACLA FEL measured 2 picoseconds after excitation for a fluence of approximately 20 mJ/cm^2 . No change in the peak position is observed within the first 4 picoseconds.

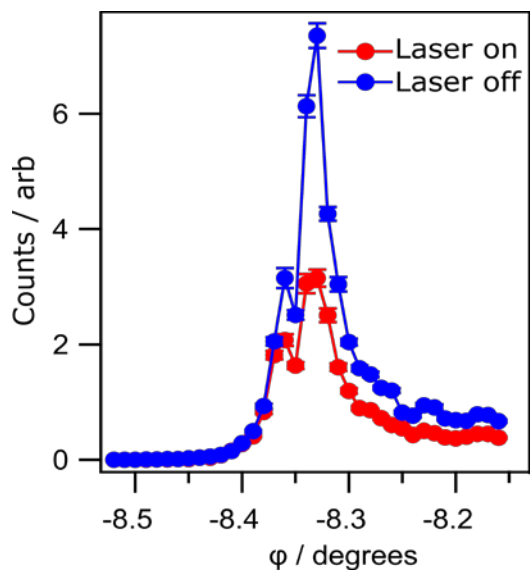


Fig. S8.

Crystal structural relations in real and reciprocal space. (a) Four twins of VO₂ and (b) Reciprocal space lattice points relation between four M1 twins and R phases (46, 47). (c) Schematic of the M1 twin2 and R phases lattice vector relation, with the Brillouin zone of the R phase (48).

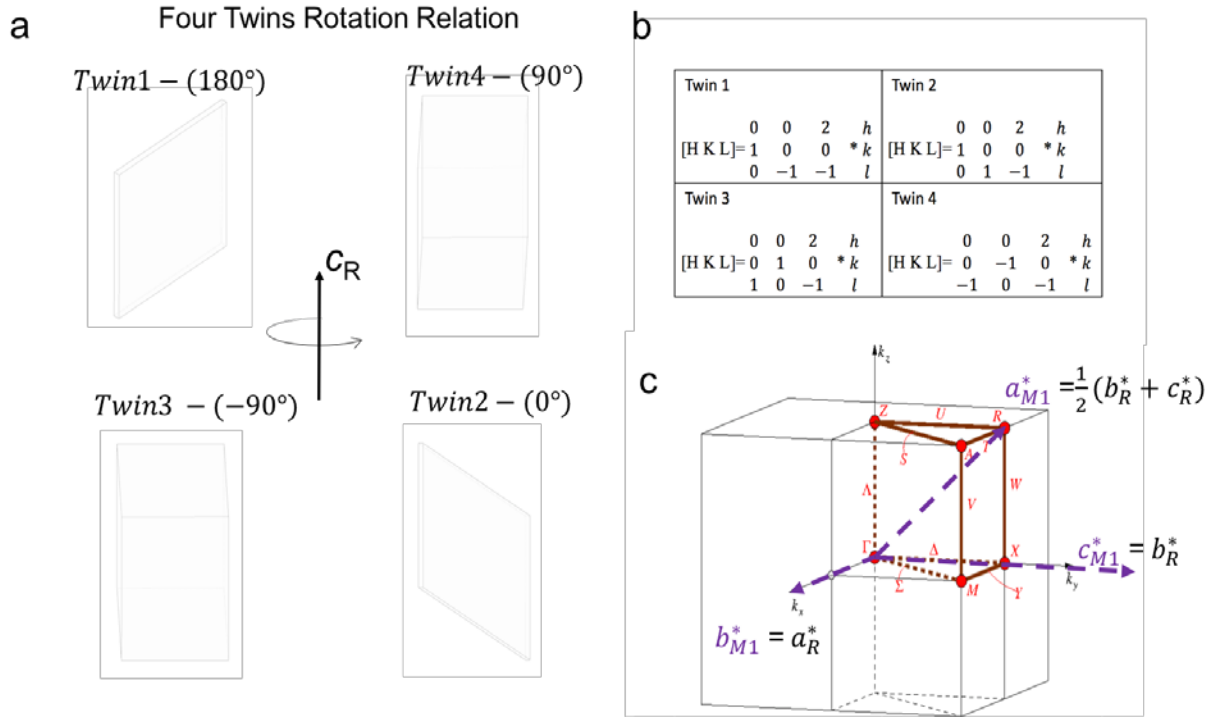


Fig. S9.

Convolution of AIMD simulation with the experimental resolution. The simulation was computed with a 1 fs step size, which is finer than the experimental resolution. To account for the finite time resolution of our setup, we convolve the simulation with 50 fs full-width half-maximum Gaussian pulses as an upper limit for the X-ray and laser resolution. The resulted convolution of the pump and probe pulses with the simulated data is shown in Fig 3, and example of the raw simulation is shown above.

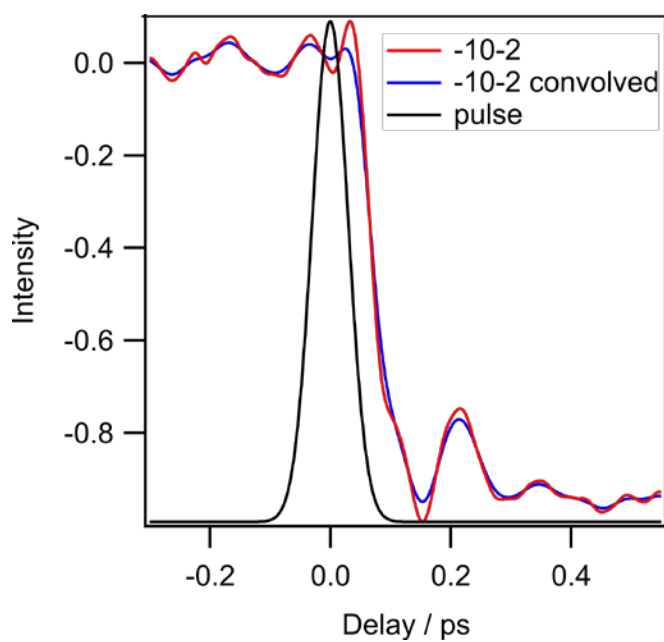


Fig. S10.

Simulated time traces of Bragg peak intensities. (a-f) are calculated with electronic occupation smearing parameter $\sigma = 0.19\text{eV}$ ($T_{el} \sim 2204\text{K}$). With $\sigma = 0.19\text{eV}$ ($T_{el} \sim 2204\text{K}$) the Bragg peaks drop down (or increase) immediately after the phonon excitation.

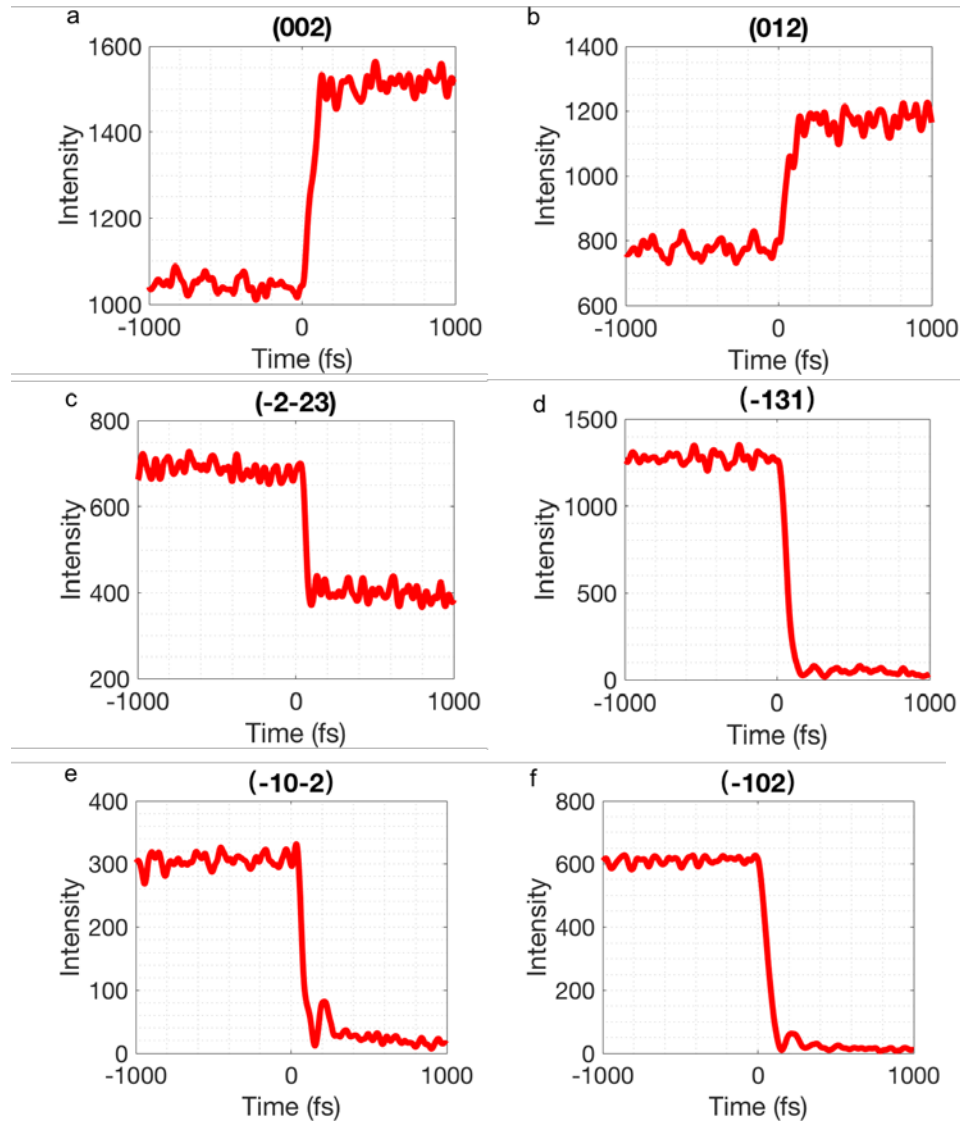


Fig S11

Coherent phonon oscillations are observed on the (-1,-3,0) Bragg peak for low fluences. The solid blue line is a fit to the response with a 5.7 THz phonon mode with an additional offset. The solid red line is a guide to the eye. At higher fluences the phonon oscillation is lost and the Bragg intensity is suppressed, in agreement to what is observed optically in ref (4).

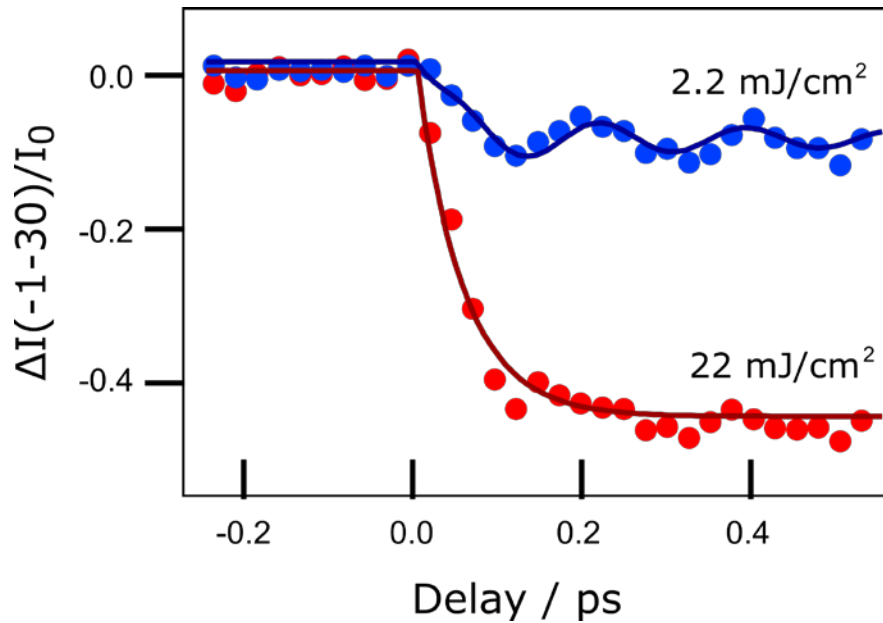
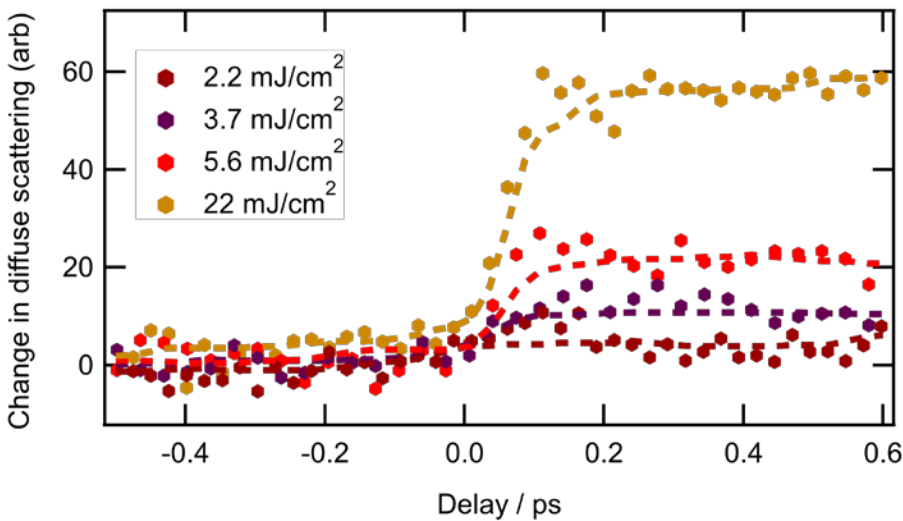


Fig. S12

Dynamics of diffuse scattering as a function of laser fluence. Dashed lines are guides to the eye.



Movie S1.

Dynamics of the photoinduced changes in the total scattering for azimuthal angle of 7 degrees.

Movie S2.

Dynamics of the photoinduced changes in the total scattering for azimuthal angle of 22 degrees.